RSC Advances

PAPER

View Article Online
View Journal | View Issue

Cite this: *RSC Adv.*, 2025, **15**, 3704

Investigation of the anticancer activity of modified 4-hydroxyquinolone analogues: *in vitro* and *in silico* studies†

Yousra Ouafa Bouone,[a] Abdeslem Bouzina, *[a] Abdelhak Djemel,[bc] Sanaa K. Bardaweel,[d] Malika Ibrahim-Ouali,[e] Boulanouar Bakchiche,[f] Farouk Benaceur[c] and Nour-Eddine Aouf[a]

A set of nitrogen-based heterocycles derived from the quinoline ring as well as cyclohexanedione and dimedone cores were subjected to *in vitro* anticancer activity evaluation against four different cancerous cell lines namely; **HCT116**, **A549**, **PC3**, and **MCF-7** respectively to colon, lung, prostate, and breast cancers. Compound **3g** presented promising results exhibiting the best IC_{50} values among the investigated compounds for the four tested cell lines. *In vitro* results were supported with *in silico* studies including molecular docking simulation in order to learn more about the binding mode of the studied derivatives with relevant drug targets in cancer treatment, namely; anaplastic lymphoma kinase and cyclin-dependent kinase 2. Compound **3g** showing the best *in vitro* results exhibited the most promising docking scores among the studied compounds. Moreover, molecular dynamics simulation was performed to the best ligand studying its stability inside the selected enzymes. Furthermore, a DFT study was performed to investigate the structural composition, electron density, and reactivity of tested compounds to identify the most important parts of the derivatives and elaborate a structure–activity relationship.

Received 10th January 2025
Accepted 31st January 2025

DOI: 10.1039/d5ra00252d

rsc.li/rsc-advances

Introduction

In the recent years, cancer and related pathologies emerged among the deadliest diseases worldwide. According to the latest GLOBACAN report updated in 2022 by the International Agency for Research on Cancer, 20 million new cases attained from cancer were reported along with 9.7 million deaths worldwide with lung cancer being the most frequent in both attainability and mortality representing 12.4% of all cancer cases and 18.7% of all deaths due to cancer. Besides lung cancer, other types like breast, colorectum, and prostate cancers were classified among the most commonly diagnosed representing 11.6%, 9.6%, and 7.3% of all global cases.[1] Alongside with harming the physical and mental health of millions of patients and families, it is recognized that carcinogenic pathologies require very long treatment incurring fees not affordable by all patients.[2] Facing cancerous diseases is nowadays a primordial challenge in view of the high mortality caused by cancer and complications related to cancer treatment. Oncology has seen huge advancements since the appearance of what is called targeted therapy with small molecules inhibitors. The latter is the treatment that directly target the main causes of cancer development that could include enzymes and proteins with dysregulation.[3] Among the most known drug targets classified as carcinogenic; the protein kinase family responsible of the phosphorylation reaction crucial in different physiological processes. Overexpression, dysregulation, mutation, and translocation of these proteins were the origin of several diseases' development especially cancerous diseases. Furthermore, in the past few years, 80 small molecules inhibiting various kinases have secured the approval of the FDA making the proteins belonging to the kinase family the most targeted proteins in cancer research.[4]

Heterocycles are a large class of compounds constituted of heteroatom-containing rings of different sizes that originate from natural sources as well as synthetic processes. These

[a]*Laboratory of Applied Organic Chemistry, Bioorganic Chemistry Group, Department of Chemistry, Sciences Faculty, Badji-Mokhtar - Annaba University, Box 12, 23000 Annaba, Algeria. E-mail: abdeslem.bouzina@univ-annaba.dz; bouzinaabdeslem@yahoo.fr*

[b]*Laboratory of Phytochemistry and Pharmacology, Department of Chemistry, Faculty of Exact Sciences and Informatics, University of Jijel, BP 98, 18000, Jijel, Algeria*

[c]*Research Unit of Medicinal Plants, RUMP, Attached to Biotechnology Research Center, CRBt, 03000 Laghouat 25000, Constantine, Algeria*

[d]*Department of Pharmaceutical Sciences, School of Pharmacy, University of Jordan, Amman 11942, Jordan*

[e]*Ensemble TPR, 52 Av. Escadrille Normandie Niémen, Marseille, 13013, France*

[f]*Laboratory of Biological and Agricultural Sciences (LBAS), Amar Telidji University, Laghouat 03000, Algeria*

† Electronic supplementary information (ESI) available. CCDC 2259912. For ESI and crystallographic data in CIF or other electronic format see DOI: https://doi.org/10.1039/d5ra00252d

compounds are known for their high efficiency in many important fields including specifically the medicinal area.[5] Among the most pharmacologically beneficial heterocycles, are those that contain one or more nitrogen atoms.[6] These latter represented, in 2020, 75% of the commercialized drugs as well as the entities approved by the FDA exhibiting various biological effects against a high number of diseases like cancer,[7,8] HIV,[9] tuberculosis,[10] alzheimer's,[11] and diabetes[12] as well as presenting excellent antimicrobial activity.[13] Quinolines and derivatives represent an integral part of the nitrogen-based interesting heterocycles presenting a remarkable number of pharmacological activities.[14] Compounds inclosing a quinoline core have been widely used in the clinical treatment of several pathologies.

As an example, chloroquine **1** was first commercialized and used as an antimalarial agent for a long time,[15] besides, it was associated later to Covid-19 treatment along with hydroxychloroquine **2** (Fig. 1).[16] Many other compounds featuring the quinoline core were employed as active substances against several health issues, such as ciproflaxin **3** and pitavastatin **4** as antibiotic and cholesterol lowering agents respectively (Fig. 1).[13,15,17]

On the other hand, six-membered heterocycles fused to non-aromatic rings such as cyclohexanedione and dimedone moieties have attracted much interest in the domain of drug design and development of novel drug candidates.[18] Numerous scientific papers were dedicated to synthesize and evaluate the biological activities of such compounds, and many of the synthesized products were found to be efficient including xanthenone **5**, chromenone **6**, hydroquinolines **7**, and acridinedione **8** displaying respectively; antimicrobial,[19] anticancer,[18] calcium channels inhibition,[20] and anti-inflammatory[21] activities (Fig. 2).

The present work is dedicated to the evaluation of the anticancer activity of modified quinoline rings consisting of 6-membered nitrogen-based heterocycles fused to cyclohexane-1,3-dione or dimedone cores. Ten derivatives of the stated family of compounds were tested against four different cancer cell lines involving **HCT116** (colon cancer), **A549** (lung cancer), **PC3** (prostate cancer), and **MCF-7** (breast cancer). The *in vitro* results were reinforced through *in silico* studies including molecular docking in which the activity of investigated compounds was predicted against two proteins belonging to the kinase family citing anaplastic lymphoma kinase and cyclin-dependent kinase 2. Furthermore, molecular dynamics simulation was performed to study the stability of the best ligand inside the cavities of both above-mentioned proteins. Additionally, a DFT complementary study was carried out to enrich our knowledge about the electronic behavior and the reactivity of the studied 4-hydroxyquinolone analogues (Scheme 1).

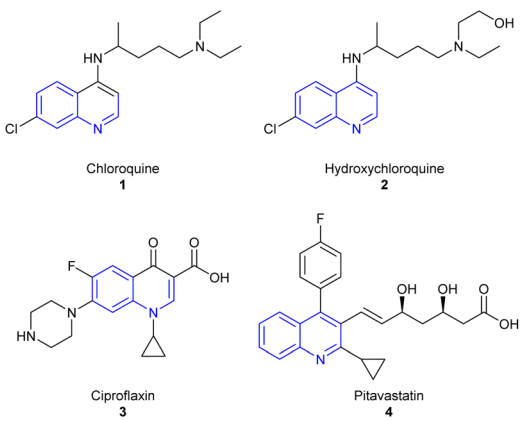

Fig. 1 Structure of commercialized active quinoline derivatives.

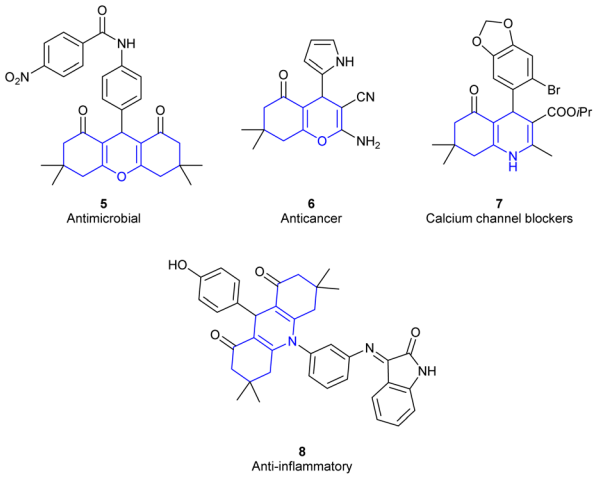

Fig. 2 Structures of dimedone-based fused heterocycles.

Experimental

Chemistry

Chemical methods. All chemicals and solvents were purchased from Sigma-Aldrich and Thermo-Fisher Scientific and were used as received without any further purification. All reactions were monitored by TLC on silica Merck 60 F_{254} percolated aluminium plates and were developed by spraying with ninhydrin solution (10% in EtOH). Proton nuclear magnetic resonance (^{1}H-NMR) spectra were recorded on a Brücker spectrometer at 400 MHz. Chemical shifts are reported in δ units (ppm) with TMS as reference (δ 0.00). All coupling constants (J) are reported in Hertz. Multiplicity is

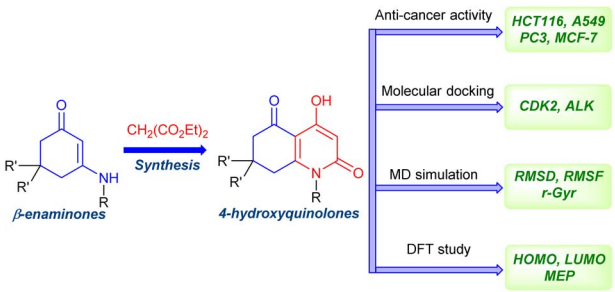

Scheme 1 Schematic representation of the design strategy employed in this work.

indicated by one or more of the following: s (singlet), d (doublet), t (triplet), p (pentet), m (multiplet), dd (doublet of doublets), td (triplet of doublets), ddd (doublet of doublets of doublets). Carbon nuclear magnetic resonance (^{13}C-NMR) spectra were recorded on a Brücker at 100 MHz. The purity of the final compounds was determined by HPLC-MS analyses and were performed on a Shimadzu Prominence LC analytical system consisting of Shimadzu LC-20AD binary HPLC pump, Shimadzu CTO-10AS column oven, Shimadzu SIL-20ACHT cooling autosampler, Shimadzu CBM-20A system controller, and Shimadzu SPD-20MA diode array detector; LC-MS-2020 mass detector with single quadrupole equipped with electrospray ionization (all Shimadzu, Kyoto, Japan). The quantification was performed on monolithic Chromolith RP-C18 column (2.1 mm × 50 mm, 1.8 μm particle size) with a gradient mobile phase of H_2O/CH_3CN (70 : 30, v/v) with 0.1% of formic acid to H_2O/CH_3CN (10 : 90, v/v) with 0.1% of formic acid at a flow rate of 0.5 mL min^{-1}, with UV monitoring at the wavelength of 254 nm with a run time of 30 min. Chemical shifts are reported in δ units (ppm) relative to $CDCl_3$ or DMSO (δ 77.0 and 39.0–40.0). Microanalysis spectra were performed by Elemental Analyser (Euro E.A. 3000-V3.0-single-2007), and the determined values were within the acceptable limits of the calculated values. Melting points were recorded on a Büchi B-545 apparatus in open capillary tubes.

X-ray diffraction analysis. Crystallographic data for the studied compound 4-hydroxy-7,7-dimethyl-1-phenyl-7,8-dihydroquinoline-2,5(1*H*,6*H*)-dione **3f** was collected on a SuperNova, Dual, Cu at home/near, AtlasS2 four-circle diffractometer equipped with an AtlasS2 CCD detector using Cu K_α (microfocus sealed tube) radiation (λ = 1.54184 Å), the crystal was kept at a temperature of 296 K during data collection.

The crystallographic data and experimental details for structural analysis are summarized in Table 1. The reported structure was solved with the SHELXT-2014/5 (ref. 22) solution program by Intrinsic Phasing with Olex2 (ref. 23) as the graphical interface. The model was refined with SHELXL-2018/3 (ref. 24) using full matrix least-squares minimization on F^2. All absorption corrections were performed with the CrysAlisPro 1.171.42.51a[25] using spherical harmonics implemented in SCALE3 ABSPACK scaling algorithm. Crystal structure visualization and construction of crystal packing diagrams were performed using Mercury 3.8 software.[26]

CCDC 2259912, contains the supplementary crystallographic data for compound **3f**. These data can be obtained free of charge from The Cambridge Crystallographic Data Centre *via* **https://www.ccdc.cam.ac.uk/data_request/cif**.

General procedure for the synthesis of β-enaminones. The synthesis of β-enaminones was done according to the method described by Redjemia *et al.*[27] In a glass tube (diameter: 25 mm; thickness: 1 mm; volume: 20 mL) taken a mixture of a dicarbonyl compound (1 mmol), an amine (1 mmol), and CuBr (0.05 mmol). The reaction mixture was subjected to ultrasonic irradiation with a frequency of 40 kHz for appropriate time at room temperature. The progress of the reaction was monitored by TLC. After completion of the reaction, DCM (5 mL) was added. The catalyst was recovered from the residue and the filtrate was concentrated. A (1/1) mixture of diethyl ether and *n*-hexane was added to the reaction mixture and pure product was crystallized to 6 °C overnight. The product was finally filtered and dried.

General procedure for the synthesis of 4-hydroxyquinolone analogues. Tested 4-hydroxyquinolone analogues were synthesized according to the method previously reported by our group.[28] In a glass tube (diameter: 25 mm; thickness: 1 mm; volume: 20 mL) introduced a mixture of diethyl malonate (3 mmol) and β-enaminone (1 mmol) in 1 mL of ethanol as a solvent. 0.2 mmol of $BiCl_3$ was added to the reaction mixture. Reaction content was subjected to microwave irradiation for appropriate time varying between 5 and 13 minutes. The progress of the reaction was monitored by TLC. After completion of the reaction, 5 mL of ethanol was added and the catalyst was recovered by filtration. Synthesized derivatives were purified through column chromatography eluted with a 1 : 1 mixture of ethyl acetate and petroleum ether. Pure layers were then concentrated under vacuum.

*4-Hydroxy-1-phenyl-7,8-dihydroquinoline-2,5(1H,6H)-dione (Scheme 2, entry **3a**).* Brown powder; 55% yield; mp = 162–164 °C; R_f = 0.35 (AcOEt/petroleum ether, 60 : 40). IR (KBr, cm^{-1}): 3261.97, 3063.51, 2943.69, 2890.57, 1710.86, 1592.00, 1574.67, 1530.95, 1492.38; ^{1}H-NMR (400 MHz, DMSO-d_6): δ = 1.91 (p, 2H, J = 6.4 Hz, CH_2), 2.43 (t, 2H, J = 6.2 Hz, CH_2–C), 2.54 (t, 2H, J = 5.6 Hz, 2H, CH_2–CO), 5.63 (s, 1H, CH), 7.23–7.42 (m, 2H, Ar-H),

Table 1 Crystallographic data and refinement parameters of compound **3f**

Moiety formula	$2(C_{17}H_{17}NO_3)$	Density (calculated) (g cm^{-3})	1.293
Sum formula	$C_{34}H_{34}N_2O_6$	Absorption coefficient (mm^{-1})	0.722
Formula weight (g mol^{-1})	566.63	F (000)	1200.0
Crystal habit, color	Prism	Crystal size (mm)	0.22 × 0.16 × 0.12
Crystal system	Yellow	2θ range for data collection (°)	7.83 to 152.696
Space group	$P2_1/n$	Reflections collected	25 203
a (Å)	11.3460(7)	Independent reflections	6077
b (Å)	16.9005(8)	R_{int}	0.0278
c (Å)	15.8105(10)	Number of parameters	386
α (°)	90	Goodness-of-fit on F^2	1.043
β (°)	106.296(7)	Final R indexes [$I \geq 2\sigma(I)$]	R_1 = 0.0395, wR_2 = 0.1062
γ (°)	90	R Indexes [all data]	R_1 = 0.0462, wR_2 = 0.1121
Volume (Å^3)	2909.9(3)	Largest difference peak and hole (e Å^{-3})	0.21/−0.17
Z, Z'	4, 0	CCDC deposition no.	2259912

7.42–7.64 (m, 3H, Ar-H), 12.71 (s, 1H, OH); ^{13}C NMR (101 MHz, DMSO-d_6): δ = 19.98, 28.86, 35.82, 95.86 (CH), 104.70, 128.14, 128.93, 129.48, 137.35, 162.12, 162.62 (N–C=O), 167.24 (C–OH), 202.53 (C=O); MS: (m/z) = 256 (M + 1); anal. calc. for $C_{15}H_{13}NO_3$ C, 70.58; H, 5.13; N, 5.49; found: C, 70.62; H, 5.10; N, 5.44.

*4-Hydroxy-1-(p-tolyl)-7,8-dihydroquinoline-2,5(1H,6H)-dione (Scheme 2, entry **3b**).* Crystal; 65% yield; mp = 222–224 °C; R_f = 0.45 (AcOEt/petroleum ether, 60 : 40). IR (KBr, cm^{-1}): 3391.87, 2957.15, 1655.76, 1607.02, 1511.88, 1441.96; ^{1}H-NMR (400 MHz, $CDCl_3$): δ = 1.97–2.03 (m, 2H, CH_2), 2.42 (s, 3H, CH_3), 2.47 (t, 2H, J = 6.2 Hz, CH_2–C), 2.57 (t, 2H, J = 6.0 Hz, CH_2–CO), 5.87 (s, 1H, CH), 7.05 (d, 2H, J = 8.2 Hz, Ar-H), 7.32 (d, 2H, J = 8.0 Hz, Ar-H), 12.43 (s, 1H, OH); ^{13}C NMR (101 MHz, $CDCl_3$): δ = 20.81, 21.36, 29.41, 36.59, 98.01 (CH), 105.98, 127.63, 130.82, 134.77, 139.70, 160.40, 164.05 (N–C=O), 167.78 (C–OH), 201.59 (C=O); MS: (m/z) = 270 (M + 1); anal. calc. for $C_{16}H_{15}NO_3$ C, 71.36; H, 5.61; N, 5.20; C, 71.31; H, 5.64; N, 5.23.

*1-(4-Chlorophenyl)-4-hydroxy-7,8-dihydroquinoline-2,5(1H,6H)-dione (Scheme 2, entry **3c**).* Crystal; 60% yield; mp = 240–242 °C; R_f = 0.62 (AcOEt/petroleum ether, 60 : 40). IR (KBr, cm^{-1}): 3258.20, 2924.99, 1673.74, 1532.55, 1489.79, 1403.58; ^{1}H-NMR (400 MHz, DMSO-d_6): δ = 1.92 (p, 2H, J = 6.3 Hz, CH_2), 2.44 (t, 2H, J = 6.2 Hz, CH_2–C), 2.54 (t, 2H, J = 6.0 Hz, CH_2–CO), 5.64 (s, 1H, CH), 7.32–7.40 (m, 2H, Ar-H), 7.58–7.66 (m, 2H, Ar-H), 12.70 (s, 1H, OH); ^{13}C NMR (101 MHz, D MSO-d_6): δ = 19.96, 28.86, 35.82, 95.81 (CH), 104.82, 129.53, 130.21, 133.64, 136.18, 162.10, 162.52 (N–C=O), 167.33 (C–OH), 202.53 (C=O); MS: (m/z) = 290 (M + 1); anal. calc. for $C_{15}H_{12}ClNO_3$ C, 62.19; H, 4.18; N, 4.83; found: C, 62.15; H, 4.14; N, 4.80.

*1-(4-Fluorophenyl)-4-hydroxy-7,8-dihydroquinoline-2,5(1H,6H)-dione (Scheme 2, entry **3d**).* Crystal; 60% yield; mp = 226–228 °C; R_f = 0.49 (AcOEt/petroleum ether, 60 : 40). IR (KBr, cm^{-1}): 3398.70, 2921.08, 1728.10, 1661.78, 1605.05, 1584.15, 1559.12, 1401.03; ^{1}H-NMR (400 MHz, $CDCl_3$): δ = 1.97–2.08 (m, 2H, CH_2), 2.48 (t, 2H, J = 6.2 Hz, CH_2–C), 2.58 (t, 2H, J = 6.0 Hz, CH_2–CO), 5.86 (s, 1H, CH), 7.13–7.19 (m, 2H, Ar-H), 7.19–7.25 (m, 2H, Ar-H), 12.43 (s, 1H, OH); ^{13}C NMR (101 MHz, $CDCl_3$): δ = 20.78, 29.45, 36.54, 98.02 (CH), 106.16, 117.17, 117.40, 129.82, 129.91, 133.19, 133.22, 160.13, 163.89 (N–C=O), 167.89 (C–OH), 201.58 (C=O); MS: (m/z) = 274 (M + 1); anal. calc. for $C_{15}H_{12}FNO_3$ C, 65.93; H, 4.43; N, 5.13; found: C, 65.99; H, 4.47; N, 5.10.

*4-Hydroxy-1-(2-methoxyphenyl)-7,8-dihydroquinoline-2,5(1H,6H)-dione (Scheme 2, entry **3e**).* Crystal; 65% yield; mp = 171–173 °C; R_f = 0.29 (AcOEt/petroleum ether, 60 : 40). IR (KBr, cm^{-1}): 3401.19, 2952.72, 1682.96, 1650.30, 1528.11, 1503.17, 1410.66; ^{1}H-NMR (400 MHz, DMSO-d_6): δ = 1.66–2.05 (m, 2H, CH_2), 2.22–2.35 (m, 2H, CH_2–C), 2.42–2.68 (m, 2H, CH_2–CO), 3.76 (s, 3H, CH_3), 5.61 (s, 1H, CH), 7.10 (td, 1H, J = 1.2, 7.6 Hz, Ar-H), 7.23 (dd, 2H, J = 1.7, 7.7 Hz, Ar-H), 7.49 (ddd, 1H, J = 1.7, 7.4, 8.3 Hz, Ar-H), 12.68 (s, 1H, OH); ^{13}C NMR (101 MHz, DMSO-d_6): δ = 19.97, 27.77, 35.82, 55.86, 95.83 (CH), 104.65, 112.57, 120.93, 125.47, 129.27, 130.72, 154.09, 162.10, 162.36 (N–C=O), 167.19 (C–OH), 202.42 (C=O); MS: (m/z) = 286 (M + 1); anal. calc. for $C_{16}H_{15}NO_4$ C, 67.36; H, 5.30; N, 4.91; found: C, 67.31; H, 5.25; N, 4.87.

*4-Hydroxy-7,7-dimethyl-1-phenyl-7,8-dihydroquinoline-2,5(1H,6H)-dione (Scheme 2, entry **3f**).* Crystal; 68% yield; mp = 210–212 °C; R_f = 0.47 (AcOEt/petroleum ether, 60 : 40). IR (KBr, cm^{-1}): 3429.88, 2963.91, 1676.72, 1592.40, 1536.24, 1455.51, 1405.54; ^{1}H-NMR (400 MHz, $CDCl_3$): δ = 1.03 (s, 6H, $2CH_3$), 2.32 (s, 2H, CH_2–C), 2.44 (s, 2H, CH_2–CO), 5.87 (s, 1H, CH), 7.13 (d, 2H, J = 7.2 Hz, Ar-H), 7.11–7.18 (m, 2H, Ar-H), 7.46–7.59 (m, 3H, Ar-H), 12.39 (s, 1H, OH); ^{13}C NMR (101 MHz, $CDCl_3$): δ = 28.14, 32.63, 42.81, 50.16, 97.91 (CH), 104.99, 128.03, 129.58, 130.26, 137.45, 158.73, 164.13 (N–C=O), 167.62 (C–OH), 201.28 (C=O); MS: (m/z) = 284 (M + 1); anal. calc. for $C_{17}H_{17}NO_3$ C, 72.07; H, 6.05; N, 4.94; found: C, 72.10; H, 6.08; N, 4.99.

*1-Benzyl-4-hydroxy-7,7-dimethyl-7,8-dihydroquinoline-2,5(1H,6H)-dione (Scheme 2, entry **3g**).* Crystal; 69% yield; mp = 168–170 °C; R_f = 0.64 (AcOEt/petroleum ether, 60 : 40). IR (KBr, cm^{-1}): 3350.20, 3031.30, 2954.97, 1659.17, 1632.99, 1586.34, 1443.85; ^{1}H-NMR (400 MHz, DMSO-d_6): δ = 0.92 (s, 6H, $2CH_3$), 2.48 (s, 2H, CH_2–C), 2.84 (s, 2H, CH_2–CO), 5.37 (s, 2H, N–CH_2), 5.68 (s, 1H, CH), 7.13 (d, 2H, J = 7.2 Hz, Ar-H), 7.25–7.30 (m, 1H, Ar-H), 7.36 (dd, 2H, J = 4.6, 10.1 Hz, Ar-H), 12.65 (s, 1H, OH); ^{13}C NMR (101 MHz, DMSO-d_6): δ = 27.33, 31.85, 45.70, 48.78, 95.58 (CH), 104.08, 125.91, 127.21, 128.69, 136.27, 160.56, 162.70 (N–C=O), 166.71 (C–OH), 202.00 (C=O); MS: (m/z) = 298 (M + 1); anal. calc. for $C_{18}H_{19}NO_3$ C, 72.71; H, 6.44; N, 4.71; found: C, 72.74; H, 6.40; N, 4.65.

*1-(4-Fluorophenyl)-4-hydroxy-7,7-dimethyl-7,8-dihydroquinoline-2,5(1H,6H)-dione (Scheme 2, entry **3h**).* Yellow powder; 70% yield; mp = 193–195 °C; R_f = 0.66 (AcOEt/petroleum ether, 60 : 40). IR (KBr, cm^{-1}): 3373.70, 2956.29, 1665.73, 1625.38, 1526.83, 1508.41; ^{1}H-NMR (400 MHz, $CDCl_3$): δ = 1.04 (s, 6H, $2CH_3$), 2.31 (s, 2H, CH_2–C), 2.44 (s, 2H, CH_2–CO), 5.85 (s, 1H, CH), 7.11–7.14 (m, 2H, Ar-H), 7.20–7.25 (m, 2H, Ar-H), 12.37 (s, 1H, OH); ^{13}C NMR (101 MHz, $CDCl_3$): δ = 28.15, 32.63, 42.89, 50.07, 97.84 (CH), 105.11, 117.27, 117.50, 129.92, 133.20, 158.68, 161.63, 164.11 (N–C=O), 167.67 (C–OH), 201.27 (C=O); MS: (m/z) = 302 (M + 1); anal. calc. for $C_{17}H_{16}FNO_3$ C, 67.76; H, 5.35; N, 4.65; found: C, 67.71; H, 5.34; N, 4.61.

*4-Hydroxy-1-(4-methoxyphenyl)-7,7-dimethyl-7,8-dihydroquinoline-2,5(1H,6H)-dione (Scheme 2, entry **3i**).* Crystal; 71% yield; mp = 186–188 °C; R_f = 0.44 (AcOEt/petroleum ether, 60 : 40). IR (KBr, cm^{-1}): 3431.97, 2960.15, 1676.28, 1609.50, 1534.74, 1510.66, 1457.69, 1403.88; ^{1}H-NMR (400 MHz, $CDCl_3$): δ = 1.03 (s, 6H, $2CH_3$), 2.34 (s, 2H, CH_2–C), 2.43 (s, 2H, CH_2–CO), 3.86 (s, 3H, CH_3), 5.86 (s, 1H, CH), 7.04 (s, 4H, Ar-H), 12.37 (s, 1H, OH); ^{13}C NMR (101 MHz, $CDCl_3$): δ = 28.15, 32.58, 42.87, 50.13, 55.68, 97.79 (CH), 104.98, 115.48, 128.98, 129.85, 159.26, 160.16, 164.41 (N–C=O), 167.55 (C–OH), 201.28 (C=O); MS: (m/z) = 314 (M + 1); anal. calc. for $C_{18}H_{19}NO_4$ C, 69.00; H, 6.11; N, 4.47; found: C, 69.04; H, 6.13; N, 4.49.

*4-Hydroxy-1-(2-methoxyphenyl)-7,7-dimethyl-7,8-dihydroquinoline-2,5(1H,6H)-dione (Scheme 2, entry **3j**).* Yellow powder; 61% yield; mp = 176–178 °C; R_f = 0.52 (AcOEt/petroleum ether, 60 : 40). IR (KBr, cm^{-1}): 3236.20, 2928.01, 1738.11, 1668.33, 1532.10, 1496.44, 1455.64; ^{1}H-NMR (400 MHz, $CDCl_3$): δ = 1.03 (d, 6H, J = 2.2 Hz, $2CH_3$), 2.23 (d, 1H, J = 17.6 Hz, CH–C), 2.36 (d, 2H, J = 17.6 Hz, CH–C), 2.43 (s, 2H, CH_2–CO), 3.80 (s, 3H, CH_3), 5.86 (s, 1H, CH), 7.04–7.17 (m, 3H, Ar-H), 7.47 (ddd, 1H, J = 3.5, 5.8, 8.3 Hz, Ar-H), 12.38 (s, 1H, OH); ^{13}C NMR (101 MHz, $CDCl_3$): δ =

27.74, 28.61, 32.47, 41.82, 50.19, 55.99, 97.76 (CH), 104.94, 112.55, 121.67, 125.90, 129.31, 131.17, 154.41, 159.75, 163.85 (N–C=O), 167.63 (C–OH), 201.31 (C=O); MS: $(m/z) = 314$ (M + 1); anal. calc. for $C_{18}H_{19}NO_4$ C, 69.00; H, 6.11; N, 4.47; found: C, 69.05; H, 6.17; N, 4.50.

Anticancer activity evaluation

The human cancer cell lines **HCT116** (colon carcinoma), **A549** (lung carcinoma), **PC3** (prostate carcinoma), **MCF-7** (breast carcinoma), and normal fibroblasts were maintained in DMEM medium, supplemented with 10% fetal bovine serum (FBS), 1% penicillin–streptomycin, and 1% L-glutamine, as previously described.[29] Cells were cultured at 37 °C in a 5% CO_2 incubator. The test compounds were dissolved in dimethyl sulfoxide (DMSO) to prepare a 10 mM stock solution. The stock was further diluted in culture medium to achieve final concentrations ranging from 0.1 μM to 500 μM, ensuring the solvent concentration did not exceed 0.1%. Cells were seeded in 96-well plates at 10 000 cells per well and incubated for 24 hours. After attachment, cells were treated with varying concentrations of the test compound and incubated for 48 hours. After treatment, 20 μL of MTT (5 mg mL^{-1}) was added to each well, and cells were incubated for 4 hours. The formazan crystals formed were dissolved in 150 μL DMSO, and absorbance was measured at 570 nm using a microplate reader.

The cytotoxicity of the compound was assessed by calculating the IC_{50} (half-maximal inhibitory concentration) using GraphPad Prism software (version 8.0).[30] Negative control cells were treated with DMSO, and positive controls were treated with cisplatin or doxorubicin. Data were presented as mean ± SD from three independent experiments ($n = 9$).

Computational methods

Molecular docking. The X-ray crystal structures of anaplastic lymphoma kinase (**ALK**) and cyclin-dependent kinase 2 (**CDK2**) in complex with Entrectinib (PDB: 5FTO),[31] and AZD5438 (PDB: 6GUE)[32] respectively obtained from the Protein Data Bank were utilized in this study. The protein structures underwent preparation using the Protein Preparation Wizard within the Schrödinger Suites software package. Three-dimensional structures of the synthesized derivatives were generated using Maestro software and further refined through optimization with Ligprep, employing the OPLS3e force field.[33] Subsequently, the prepared PDB files and synthesized compounds were subjected to the docking process. Docking simulations were performed using Glide software using standard precision (SP) function.[34] The output files containing the docked compounds bound to the protein were visualized using Chimera X[35] giving the disposition of studied compounds within the receptors as well as the interactions with the active site.

Molecular dynamics simulation. The molecular dynamics (MD) simulations were performed using Desmond on the Schrödinger Academic Software 2023-4, utilizing the OPLS-2005 force field.[36] The simulations were conducted in a Linux environment, powered by an Intel Core i5-13400F CPU at 4.60 GHz and an Nvidia GeForce RTX 3060 12GB GPU. Initial coordinates for the docking complexes **3g-ALK** and **3g-CDK 2** were employed. A 10 Å orthorhombic box with dimensions of 10.0 × 10.0 × 10.0 nm^3, utilizing the TIP3P model, included 9982 water molecules/34705 atoms for **3g-ALK** and 10 084 water molecules/35 131 atoms for **3g-CDK2**. To neutralize the system, sodium and chloride ions were added as counterions. Following solvation, energy minimization was performed with a convergence threshold of 1 kcal mol^{-1} $Å^{-1}$, succeeded by pre-equilibration through the six-step relaxation protocol of Desmond. The first two steps involved energy minimization; initially restraining the solute, then removing these restraints followed by three short MD simulations lasting 12 ps, 12 ps, and 24 ps, respectively, under *NPT* ensemble conditions at temperatures of 10 K and 300 K. A subsequent 300 ns production run was conducted under periodic boundary conditions and isothermal–isobaric conditions with a relaxation time of 0.2 ps. Visualization of the protein–ligand complexes and analysis of the MD trajectory were carried out using Maestro. In-depth analyses were conducted using Simulation Interactions Diagram, offering a comprehensive exploration of the simulation data.[37]

DFT study. Molecular geometry of the gas phase structure optimization of 4-hydroxyquinolone analogues derivatives (**3a–3j**) was performed using DFT at B3LYP method,[38] with the basis set of 6-31G(d,p) implemented by Gaussian 09 package.[39] Frontier molecular orbitals and global reactivity descriptors, the highest occupied molecular orbital (HOMO) and lowest unoccupied molecular orbital (LUMO),[40] energy gap and chemical reactivity descriptors are calculated at DFT/B3LYP/6-31G(d,p) method.

Results and discussion

Chemistry

The synthesis of interesting products using microwave irradiation[41] in addition to their biological evaluation[42,43] against multiple drug targets together with our interest grabbed by the remarkable versatility of β-enaminones as precursors to medicinally effective molecules and reactive chemical intermediates[44,45] constituted the main axis of our previous works. In this study, we aim to extend this research by exploring the anticancer activity of prepared β-enaminone-derived N-heterocycles similar to 4-hydroxyquinolone ring.

The general method for synthesizing these 4-hydroxyquinolone analogues **3(a–j)** is evocated in Scheme 2. This protocol that is advantaged with its rapidity and respect for the environment is based on the condensation of simple and available reagents; namely previously prepared β-enaminones **1(a–j)** and commercialized diethyl malonate **2** in the presence of ethanol. Reaction mixture was then subjected to microwave irradiation as an activation tool under the catalysis of bismuth chloride ($BiCl_3$).[28]

X-ray diffraction analysis

Suitable crystals of compound **3f** were subjected to a total structural elucidation using a single crystal X-ray diffraction method.

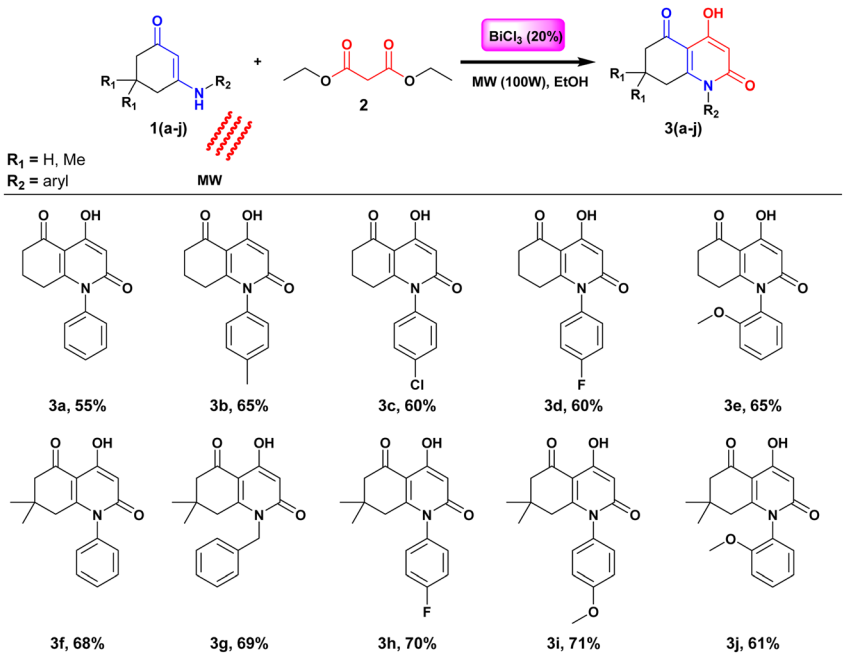

Scheme 2 Synthesis of modified 4-hydroxyquinolone analogues.

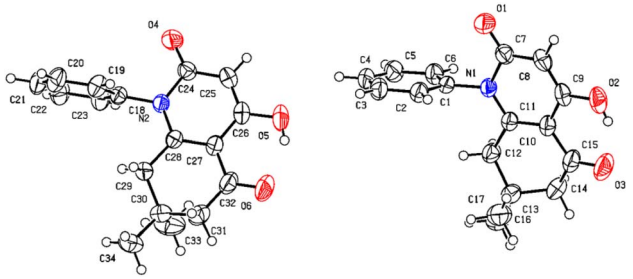

Fig. 3 ORTEP diagram for compound **3f**.

The resulting ORTEP diagram was drawn at 50% probability and is depicted in Fig. 3. Results showed that compound **3f** 4-hydroxy-7,7-dimethyl-1-phenyl-7,8-dihydroquinoline-2,5(1*H*,6*H*)-dione crystallized in the monoclinic crystal system with $P2_1/n$ space group as two molecules constituting the asymmetrical unit. The presence of the hydroxyl group allowed the formation of an intramolecular hydrogen bond with the ketone group of the adjacent cycle in both molecules of the asymmetrical unit forming two six-membered pseudocycles with S(6) graph sets. Distances of the stated hydrogen bonds were found to be in the range of 1.79 and 1.81 Å (Table 2). These observations are consistent with our previously reported crystal structure of an analogue of the same set.[28]

Several intermolecular hydrogen bonds were noticed in the crystal structure of compound **3f** as shown in the crystal packing diagram (Fig. 4), with distances ranging between 2.41 and 2.70 Å (Table 2). The observed contacts permitted the reinforcement of the crystal components keeping the cohesion of the crystal.

Anticancer evaluation

The anticancer activity of the modified 4-hydroxyquinolone analogues was assessed *in vitro* against four human cancer cell lines: **HCT116** (colon carcinoma), **A549** (lung carcinoma), **PC3** (prostate carcinoma), and **MCF-7** (breast carcinoma). The IC_{50} values, which represent the concentration of the compound required to inhibit 50% of cell viability, were determined for each compound across these cell lines (Table 3).

Compound **3a** showed relatively high IC_{50} values, ranging from 148.3 μM in **HCT116** to 189 μM in **MCF-7**, indicating

Table 2 Distances (Å) and angles (°) of hydrogen bonds for compound **3f**

D–H···A	*d*(D–H)	*d*(H···A)	*d*(D–A)	D–H–A	Symmetry
O_2–H_2···O_3	0.820	1.798	2.538(2)	149.25	*x*, *y*, *z*
O_5–H_{5A}···O_6	0.820	1.805	2.542(2)	148.8	*x*, *y*, *z*
C_6–H_6···O_2	0.930	2.452	3.356(2)	163.80	*x*, *y*, *z*; −*x*, 1 − *y*, 2 − *z*
C_2–H_{2A}···O_4	0.930	2.411	3.283(2)	156.17	*x*, *y*, *z*; −1 + *x*, *y*, *z*
C_{17}–H_{17B}···O_6	0.960	2.685	3.644(2)	177.3	*x*, *y*, *z*; −*x*, 1 − *y*, 1 − *z*
C_{29}–H_{29B}···O_1	0.970	2.598	3.234(2)	123.26	*x*, *y*, *z*; −1/2 + *x*, 1.5 − *y*, 1/2 + *z*
C_{19}–H_{19}···O_1	0.930	2.699	3.480(2)	142.13	*x*, *y*, *z*; −1/2 + *x*, 1.5 − *y*, 1/2 + *z*
C_{31}–H_{31A}···O_4	0.970	2.519	3.436(2)	157.6	*x*, *y*, *z*; −1/2 + *x*, 1.5 − *y*, −1/2 + *z*

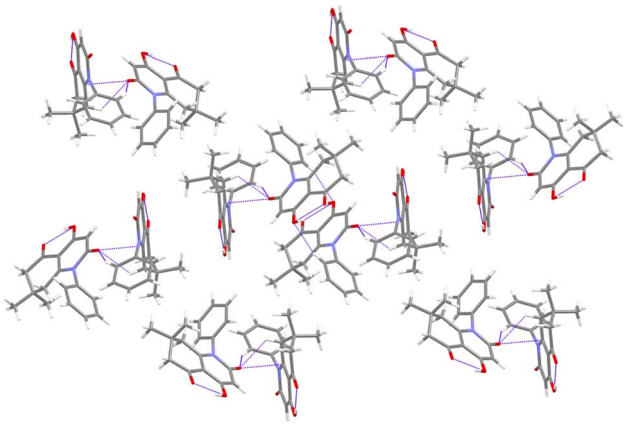

Fig. 4 Packing diagram viewed along (*a*) axis.

Table 3 IC_{50} values of tested modified 4-hydroxyquinolone analogues for anticancer activity[a]

Entry	HCT116	A549	PC3	MCF-7	Fibroblasts
3a	148.3	189.0	151.0	189.0	>500
3b	162.0	159.0	239.4	213.1	>500
3c	139.4	257.0	250.6	260.9	>500
3d	46.5	98.5	65.9	34.2	>500
3e	29.5	67.0	45.0	62.6	>500
3f	118.0	127.0	95.5	70.6	>500
3g	18.4	32.4	29.1	26.9	>500
3h	28.9	87.9	29.3	32.4	>500
3i	33.4	73.0	34.1	50.1	>500
3j	38.2	78.8	43.6	81.4	>500
Doxorubicin	5.8	—	—	2.3	—
Cisplatin	—	17.0	23.5	—	—

[a] SD never exceeded 5%. Data was collected for triplicates in three independent experiments, $n = 9$.

moderate activity. Similarly, compound **3b** exhibited IC_{50} values of 162.0 μM (**HCT116**) to 239.4 μM (**PC3**), suggesting selective but moderate efficacy.

Compound **3d** exhibited a potent anticancer activity, with IC_{50} values as low as 34.2 μM in **MCF-7** and 46.5 μM in **HCT116**, suggesting strong inhibition of cell proliferation across all tested lines. Compound **3e** also showed significant activity, with IC_{50} values ranging from 29.5 μM in **HCT116** to 67.0 μM in **A549**, indicating its potential as an effective anticancer agent. Compound **3h** exhibited IC_{50} values of 87.9 μM in **A549** and 29.3 μM in **PC3**, while compound **3i** showed promising effects with IC_{50} values ranging from 33.4 μM in **HCT116** to 73.0 μM in **A549**. Compound **3j** demonstrated moderate activity, with IC_{50} values ranging from 38.2 μM in **HCT116** to 81.4 μM in **MCF-7**.

Finally, compound **3g** exhibited the most potent anticancer activities across the cell lines, with IC_{50} values significantly lower than those of the other analogs, making it a promising candidate for further development in anticancer therapies. Importantly, the IC_{50} values of compound **3g** are comparable to those of the clinically approved standard drugs, doxorubicin and cisplatin, as shown in Table 3.

All compounds (**3a–3j**) were also tested against normal fibroblast cells to evaluate their potential toxicity. At the examined concentrations, no significant cytotoxicity was observed in the normal fibroblast cells, indicating that the compounds did not exhibit harmful effects on non-cancerous cells within the tested concentration range.

In silico study

Molecular docking. Cell lines employed in the *in vitro* study citing **HCT116**, **A549**, **PC3**, and **MCF-7** are related respectively to colon, lung, prostate, and breast cancers. Several derivatives were relatively able to inhibit the growth of cited cell lines. In order to move our research into a more specified aspect of cancer treatment which is the targeted therapy using small molecule inhibitors, it is crucial to predict the effect of investigated products on drug targets associated with the cited types of cancer using molecular docking.

To this end, we selected two known drug targets highly linked to tumor growth; firstly, the anaplastic lymphoma kinase; an insulin receptor protein belonging to the superfamily of tyrosine kinase[46] that participates in the pathogenesis of different diseases especially the NSCLC that refers to the non-small cell lung cancer presenting nearly 90% of lung cancers.[47] Secondly, the cyclin-dependent kinase 2 that is widely partitioned in the human organism plays crucial roles in cell cycle transition and is a part of many cancers development due to abnormalities such as breast, lung, colorectal, prostate, and cervical carcinomas.[48]

A molecular docking study was guaranteed employing PDB files 5FTO and 6GUE corresponding to **ALK** in complex with Entrectinib and **CDK2** in complex with AZD5438 respectively.

After completion of the molecular docking process, we were able to collect the docking scores of different investigated products inside the cavities of **ALK** and **CDK2** (Table 4). Being reliable numerical indicators of ligand–protein stability, docking score values allowed the identification of the best ligands among the studied modified 4-hydoxyquinolones.

Docking scores of simulated ligand–protein complexes corresponding to the **ALK** protein ranged between −7.19 and −9.07 kcal mol^{-1} indicating an acceptable to good stability of our products inside the active site of **ALK** compared to the reference re-docked ligand, especially for the benzyl-containing compound **3g** having the best score (−9.07 kcal mol^{-1}). Most 4-hydroxyquinolone analogues derived from dimedone-based β-enaminones exhibited better affinities according to their docking score values which suggests a significant importance of the two methyl groups contained in their structures in enhancing the stability. In addition, several interactions including H-bonds were observed between the studied compounds and the residues of the **ALK** pocket contributing to the enhancement of their stability. Compounds **3c** and **3d** containing chlorine and fluorine respectively were implicated in one H-bond with Met1199. Further, compounds **3a**, **3b**, and **3g** exhibiting the best docking score were involved in two H-bonds formation with both Met1199 and Glu1197 (Table 5) which are considered key residues of the active site since the co-crystalized

Table 4 Docking scores and observed interactions between the docked 4-hydroxyquinolone analogues and the cavities of ALK and CDK2 enzymes

	ALK (5FTO)			**CDK2** (6GUE)		
Entry	Docking scores (kcal mol^{-1})	H-bonds	Hydrophobic interactions	Docking scores (kcal mol^{-1})	H-bonds	Hydrophobic interactions
3a	−7.706	Met1199, Glu1197	Leu1122, Leu1256, Val1130, Phe1127, Ala1148, Val1180, Leu1196, Leu1198, Met1199	−7.897	Leu83	Ala144, Ala31, Val18, Tyr15, Ileu10, Val64, Phe80, Phe82, Leu83, Leu134
3b	−7.697	Met1199, Glu1197	Leu1122, Leu1256, Val1130, Phe1127, Ala1148, Val1180, Leu1196, Leu1198, Met1199	−7.612	Leu83	Ala144, Ala31, Val18, Tyr15, Ileu10, Val64, Phe80, Phe82, Leu83, Leu134
3c	−7.731	Met1199	Leu1122, Leu1256, Val1130, Phe1127, Ala1148, Val1180, Leu1196, Leu1198, Met1199	−7.705	Leu83	Ala144, Ala31, Val18, Tyr15, Ileu10, Val64, Phe80, Phe82, Leu83, Leu134
3d	−7.192	Met1199	Leu1122, Leu1256, Val1130, Phe1127, Ala1148, Leu1196, Leu1198, Met1199	−7.993	Leu83	Ala144, Ala31, Val18, Tyr15, Ileu10, Val64, Phe80, Phe82, Leu83, Leu134
3e	−7.471	—	Leu1122, Phe1127, Val1130, Leu1256, Ala1200, Met1199, Leu1198, Leu1196, Ala1148	−7.770	Leu83	Ala144, Ala31, Val18, Tyr15, Ileu10, Val64, Phe80, Phe82, Leu83, Leu134
3f	−7.935	Arg1253	Leu1122, Leu1256, Val1130, Phe1127, Ala1148, Leu1196, Met1199	−7.982	Lys33	Ala144, Ala31, Val18, Tyr15, Ileu10, Val64, Phe80, Phe82, Leu83, Leu134
3g	−9.070	Met1199, Glu1197	Leu1122, Leu1256, Val1130, Phe1127, Ala1148, Val1180, Leu1196, Leu1198, Met1199, Cys1255	−8.233	Lys33, Leu83, Asp145	Ala144, Ala31, Val18, Tyr15, Ileu10, Val64, Phe80, Phe82, Leu83, Leu134
3h	−8.266	Arg1253	Leu1122, Leu1256, Val1130, Phe1127, Ala1148, Leu1196, Leu1198, Met1199	−8.028	Lys33	Ala144, Ala31, Val18, Tyr15, Ileu10, Val64, Phe80, Phe82, Leu83, Leu134
3i	−7.451	—	Leu1122, Leu1256, Val1130, Phe1127, Ala1148, Ala1200, Leu1196, Leu1198, Met1199	−7.889	Lys33	Ala144, Ala31, Val18, Tyr15, Ileu10, Val64, Phe80, Phe82, Leu83, Leu134
3j	−7.920	Arg1253	Leu1122, Leu1256, Val1130, Phe1127, Ala1148, Leu1196, Leu1198, Met1199	−7.126	Lys33	Ala144, Ala31, Val18, Tyr15, Ileu10, Val64, Phe80, Phe82, Leu83, Leu134, Ileu135
Entrectinib	−11.966	Met1199, Glu1197	Leu1122, Leu1256, Val1130, Phe1207, Ala1148, Ala1200, Leu1196, Leu1198, Met1199, Cys1255, Pro1260	—	—	—
AZD5438	—	—	—	−10.580	Lys33, Leu83, Asp86	Ala144, Ala31, Val18, Tyr15, Ileu10, Val64, Phe80, Phe82, Leu83

ligand Entrectinib exhibited H-bonds with the same two residues. Further, the stability of the studied compounds inside the cavity of **ALK** was enhanced by significant hydrophobic interactions with several key residues including Leu1122, Leu1256, Val1130, Phe1127, Ala1148, Ala1200, Leu1196, Leu1198, Met1199, and Cys1255. Compounds **3f**, **3h**, and **3j** engaged in Pi–Pi stacking with the side chain of Phe1127 (Tables 4 and S1 ESI†).

In the case of **CDK2**, results were comparable to the **ALK** results with docking scores lying from −7.12 to −8.24 kcal mol^{-1} which corresponds to acceptable values of affinities. As noticed in the docking study using **ALK** as the target, compound **3g** exhibited the best results in the docking study involving **CDK2** as well. Compounds **3a**, **3b**, **3c**, **3d**, and **3e** displayed an H-bond with Leu83 residue, besides, derivatives **3f**, **3h**, **3i**, and **3j** were able to contribute to H-bond formation with Lys33. Among the studied compounds only derivative **3g** presenting the best docking score succeeded in the formation of 3 H-bonds with Leu83, Lys33, and Asp145. It is important to point out that the co-crystalized ligand AZD5438 also exhibited 3 H-bonds with Leu83, Lys33, and Asp86 making compound **3g** the most analogous to the reference ligand in terms of demonstrated interactions. Besides, all compounds were involved in important hydrophobic interactions with key residues of the **CDK2** active site (Ala144, Ala31, Val18, Tyr15, Ileu10, Val64, Phe80, Phe82, Leu83, Leu134, and Ileu135) contributing in the stability of the formed ligand-protein complexes (Tables 4 and S1 ESI data†).

According to the promising results and to optimize the studied derivatives as effective drug candidates with enhanced

Table 5 3D views of compounds **3(a,d,e,g,h)** inside the cavities of **ALK** (PDB: 5FTO) and **CDK2** (PDB: 6GUE) enzymes (H bonds are represented as black dashed lines)

	Drug targets	
Entry	**ALK** (PDB: 5FTO)	**CDK2** (PDB: 6GUE)
3a	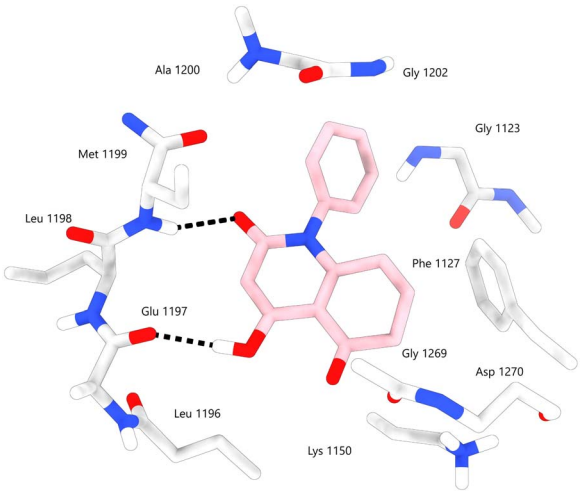	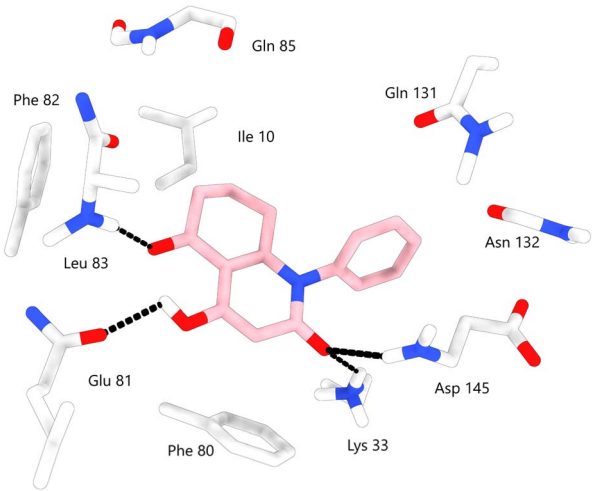
3d	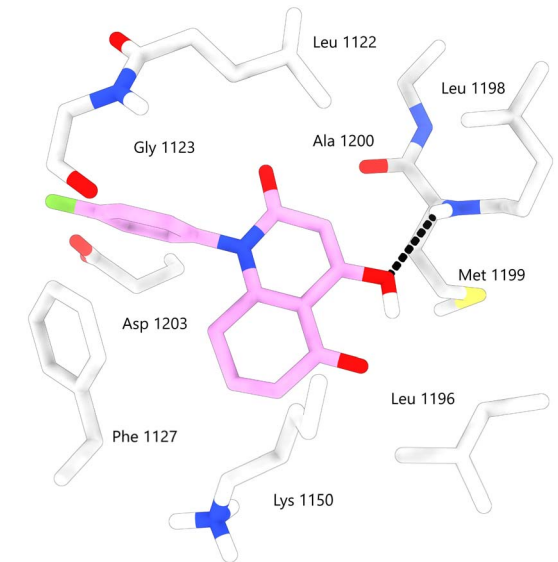	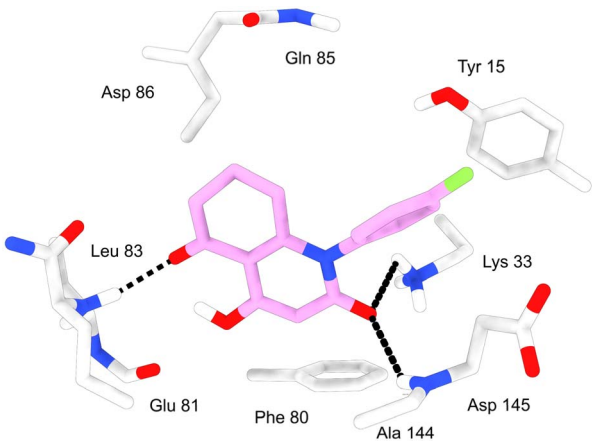
3e	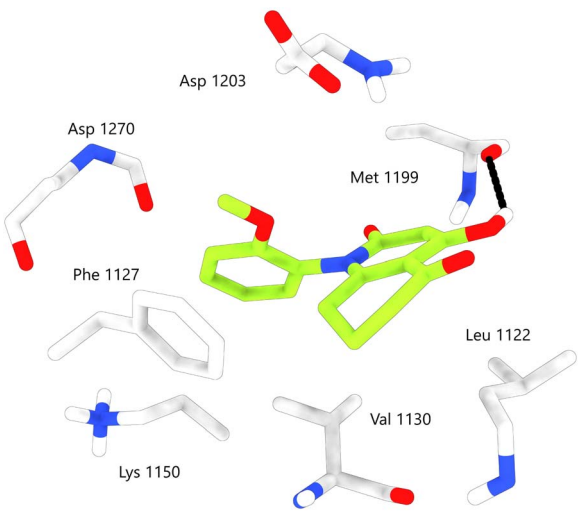	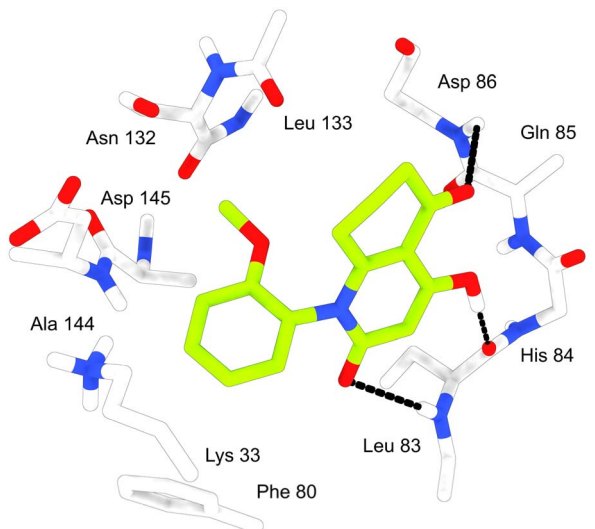

Table 5 (*Contd.*)

Entry	Drug targets	
	ALK (PDB: 5FTO)	**CDK2** (PDB: 6GUE)
3g	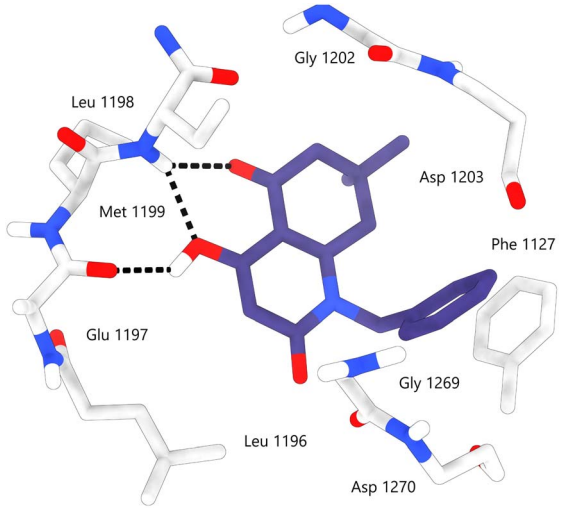	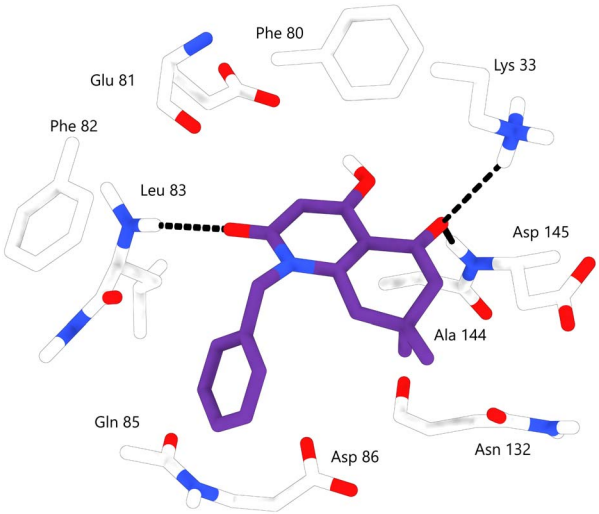
3h	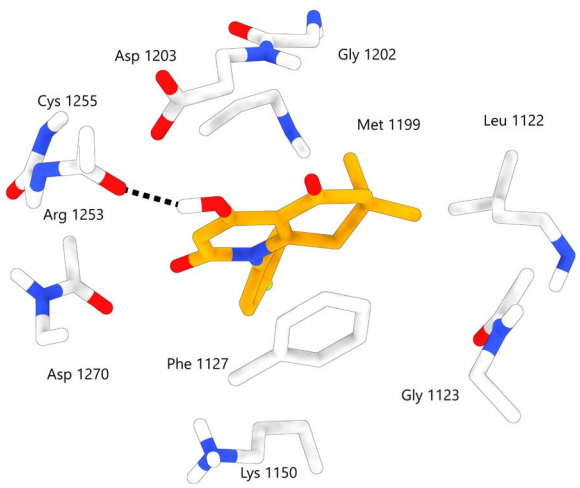	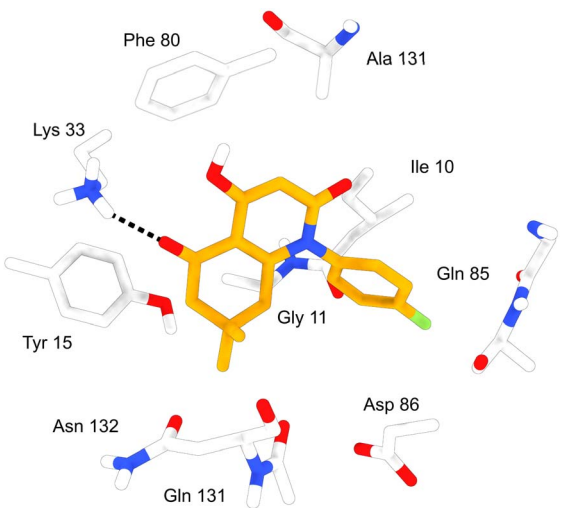

activity, we propose modifying the substitutions on the nitrogen atom. Notably, the **3g** derivative exhibits the highest activity in both *in vitro* and *in silico* studies. This increased activity is likely attributed to the structural difference in **3g**, where a methylene group separates the nitrogen atom from the aromatic nucleus, unlike the other derivatives.

This separation reduces steric hindrance, allowing the **3g** molecule to position itself more effectively within the active site pockets of **CDK2** and **ALK**. Consequently, we are exploring the use of aliphatic or aromatic amines linked *via* side chains to further improve activity.

Molecular dynamics simulation. The MD simulation aimed to evaluate the structural stability, dynamics, and interaction profile of the ligand **3g** in the active pocket of the two studied proteins **ALK** and **CDK2** under near-physiological conditions (NPT ensemble at 300 K). With a total simulation time of 300 ns, the two systems provided a comprehensive trajectory to assess equilibrium states and molecular interactions. Key features included a neutral ligand, counterions for charge neutrality, and explicit water molecules to mimic the biological environment. These settings ensure a realistic evaluation of protein–ligand dynamics.

The RMSD plot for the **3g-ALK** complex demonstrated remarkable stability, with minimal fluctuations observed in the protein structure. These small variations suggest that the protein likely stabilized around a consistent thermal average

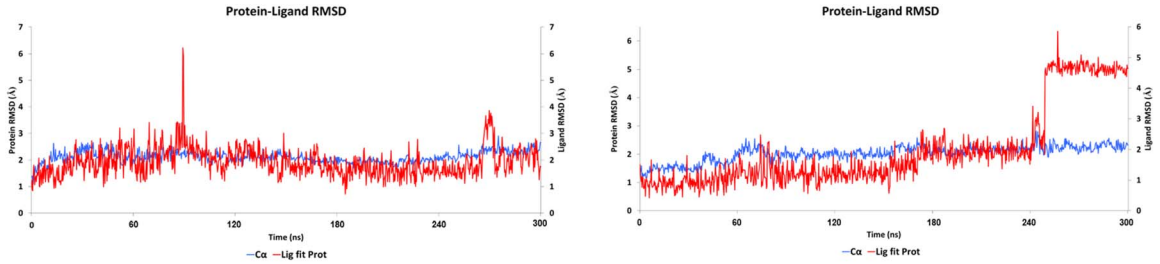

Fig. 5 RMSD (3g-ALK: left, 3g-CDK2: right).

during the second half of the simulation. This behavior indicates that the protein reached equilibrium, a critical prerequisite for the meaningful interpretation of binding interactions and conformational analyses.

Notably, the RMSD range for the system did not exceed 0.2 Å. Similarly, the RMSD plot for the ligand exhibited a highly stable trajectory, indicating that the ligand remained securely bound to the protein's active site without significant displacement. This observed stability strongly supports the high affinity of the **3g** ligand and its proper fit within the binding pocket of the **ALK** enzyme (Fig. 5).

For the second system, **3g-CDK2**, the ligand demonstrated significant stability within the active pocket throughout the simulation. From 0 to 250 ns, the alignment between the C-alpha atoms and the ligand-fitted protein was highly stable, with the RMSD remaining close to 0 Å. After 250 ns, a slight deviation in the ligand was observed, with the RMSD increasing to 2.5 Å. Despite this deviation, the RMSD consistently stayed below 3 Å, indicating that the ligand maintained stable interactions within the binding site across the entire simulation.

These findings underscore the strong affinity and stability of ligand **3g** for **CDK2** enzyme. The minimal fluctuations and sustained alignment suggest that forms strong interactions with the active site without disrupting the structural integrity of the protein. This consistent stability highlights the ligand's potential for targeted therapeutic applications, as it maintains its binding efficiency and supports the functional conformation of protein throughout the simulation period (Fig. 5).

In the analysis of the obtained results for the two studied systems, **3g-ALK** and **3g-CDK2**, no significant fluctuations were observed in the curve of the atomic displacement, indicating consistency between simulated and experimental flexibility metrics.

These findings confirm the success of the simulation, as the RMSF and *B*-factor curves remained parallel throughout most of the 300 ns trajectory. The overall RMSF patterns for both **ALK** and **CDK2** systems demonstrated structural stability during the simulation. Notably, residues critical for ligand binding exhibited low RMSF values in both systems, indicating that the ligand **3g** effectively stabilized the binding pockets of the enzymes.

Additionally, both systems showed an RMSF range within acceptable limits for stable proteins, with significant flexibility restricted to loop regions and terminal residues. This localized flexibility likely facilitates the functional dynamics of the proteins while preserving their overall structural integrity (Fig. 6).

The radius of gyration (rGyr) reflects the spatial distribution of a molecule's atoms around its center of mass. For ligands, rGyr provides insights into compactness and conformational changes during a simulation. A lower rGyr indicates that the ligand adopts a more compact and stable conformation, which is generally favorable for binding as compact ligands tend to fit more snugly into binding pockets. Variations in rGyr over the simulation reflect flexibility. While moderate flexibility can enable the ligand to adapt to the binding pocket of the protein, excessive flexibility might indicate instability. The rGyr results for ligand **3g** in the active pockets of the two studied enzymes, **ALK** and **CDK2**, demonstrated significant stability during the 300 ns simulations. In both systems, the rGyr remained consistently within the range of 3.5–3.8 Å, with a very small deviation of approximately 0.3 Å. This limited fluctuation suggests that the ligand **3g** maintained a stable and compact conformation throughout the simulation (Fig. 7).

All contacts identified through molecular docking were preserved during molecular dynamics simulations for the two studied complexes, **3g-ALK** and **3g-CDK2**, indicating the reliability of the molecular docking results. For the **ALK** enzyme, ligand **3g** demonstrated the formation of three hydrogen bonds observed in the docking study, along with an additional

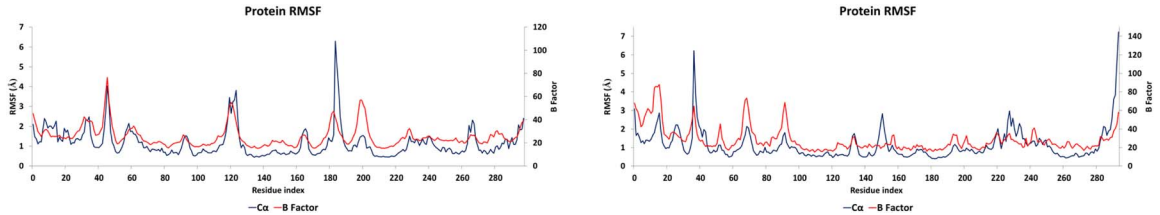

Fig. 6 RMSF (3g-ALK: left, 3g-CDK2: right).

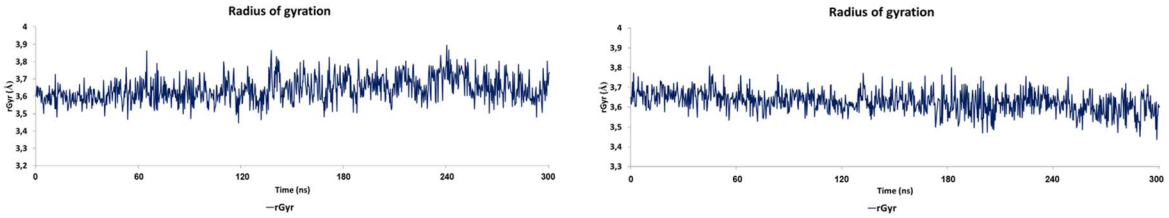

Fig. 7 Radius of gyration (**3g-ALK**: left, **3g-CDK2**: right).

hydrogen bond involving Lys 1150 and the carbonyl oxygen, with a persistence rate of 42%. This residue also participated in a Pi–cation interaction with the benzylic ring at 21%. Additionally, all hydrophobic interactions identified during docking were maintained throughout the simulation.

For the **CDK2** target, ligand **3g** retained the three hydrogen bonds observed in the molecular docking study and formed an additional hydrogen bond with Glu 81. Furthermore, ligand **3g** exhibited strong hydrophobic interactions with key residues, including Leu 134, Tyr 15, Ala 131, and other residues within the active pocket of **CDK2**. These interactions highlight the stability of ligand **3g** within the binding sites of **CDK2**, further validating its potential as a therapeutic candidate (Fig. 8).

DFT study. Molecular descriptors and different parameters of the studied 4-hydroxyquinolone analogues were generated according to the DFT B3LYP 6-31G(d,p) method as shown in Table 6.

Dipolar moments of investigated compounds ranged between 2.5369 and 7.3766 D starting from the chlorine-substituted derivative **3c** to the methoxy-substituted derivative **3i** as the less and most polar compounds respectively. Optimized structures and FMOs graphical representations of all synthesized 4-hydroxyquinolone analogues are summarized in Table 7.

The energy gap values between HOMO and LUMO for studied compounds were located in the interval of [3.9046–4.7838 eV], in which compound **3g** is the most stable among studied derivatives.

Additionally, HOMO and LUMO orbitals as presented in Table 7 are situated in the key functional groups of the heterocyclic core of the investigated compounds including the amide and the enolic part as well as the carbonyl of the cyclohexene ring suggesting a high ability of these parts to donate and accept electrons permitting their interactions with molecular targets through electron transfer.

MEP of investigated compounds were represented as maps with color codes lying between the deepest red showing the most nucleophilic parts and the deepest blue showing the most electrophilic ones (Fig. 9).Generally, red color was situated in the carbonyl groups corresponding to ketone and amide moieties. It can be assumed that these groups have a high potency to form interactions by acting as proton acceptors in H-

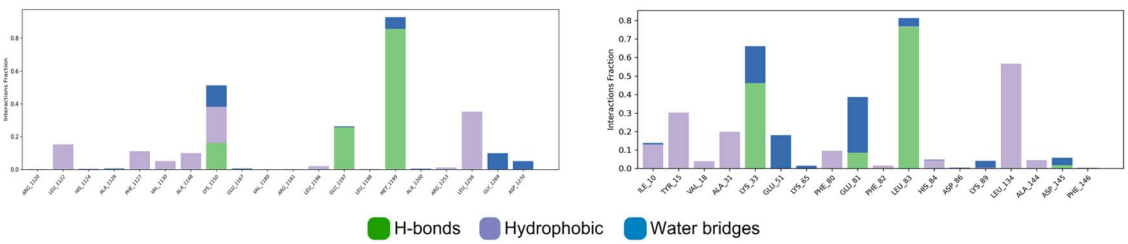

Fig. 8 *P–L* contacts (**3g-ALK**: left, **3g-CDK2**: right).

Table 6 Molecular descriptors and parameters of studied 4-hydroxyquinolone analogues

Entry	μ (D)	E_{HOMO} (eV)	E_{LUMO} (eV)	ΔE_{gap}	(η)	(S)	(μ)	(χ)	(ω)
3a	4.0139	−5.9601	−1.2267	4.7334	2.3667	0.4225	−3.5934	3.5934	2.7279
3b	4.4347	−5.9171	−1.1823	4.7348	2.3674	0.4224	−3.5497	3.5497	2.6613
3c	2.5369	−6.1011	−1.3818	4.7193	2.3596	0.4238	−3.7414	3.7414	2.9662
3d	2.8784	−6.0475	−1.3124	4.7351	2.3675	0.4224	−3.6799	3.6799	2.8599
3e	4.9604	−5.8115	−1.0754	4.7361	2.3681	0.4223	−3.4435	3.4435	2.5036
3f	4.0406	−5.9416	−1.2104	4.7312	2.3656	0.4227	−3.5760	3.5760	2.7028
3g	3.4627	−5.9977	−1.2139	4.7838	2.3919	0.4181	−3.6058	3.6058	2.7179
3h	2.9442	−6.0279	−1.2961	4.7318	2.3659	0.4227	−3.6620	3.6620	2.8340
3i	7.3766	−5.8115	−1.5742	4.2374	2.1187	0.4720	−3.6929	3.6929	3.2183
3j	4.7610	−8.9558	−5.0513	3.9046	1.9523	0.5122	−7.0035	7.0035	12.5621

Table 7 HOMO and LUMO orbitals for synthesized 4-hydroxyquinolone analogues

Code	Optimized structure	HOMO	LUMO
3a	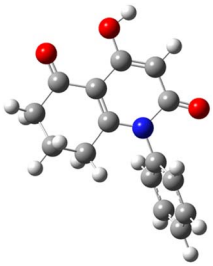	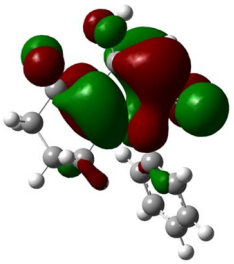	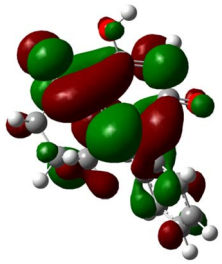
3b	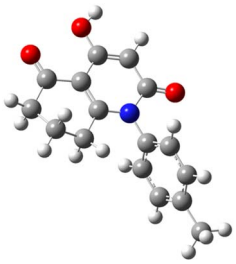	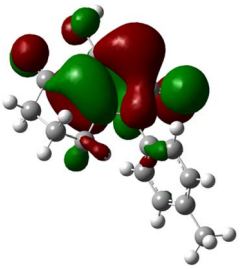	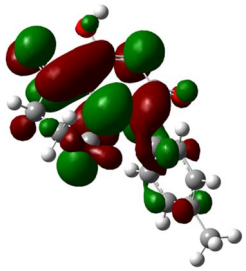
3c	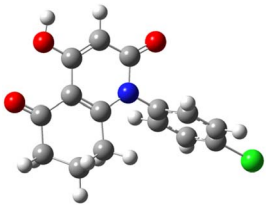	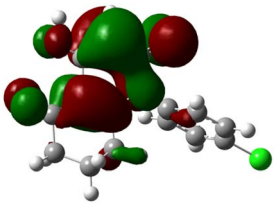	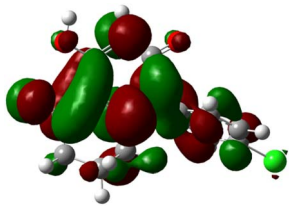
3d	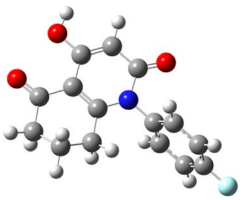	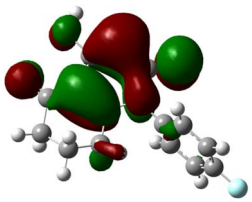	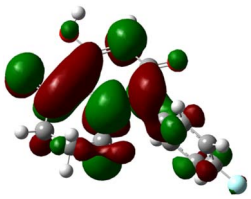
3e	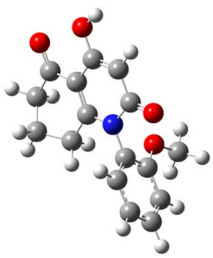	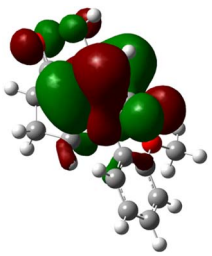	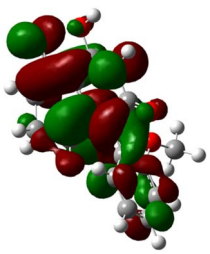
3f	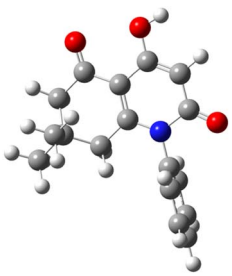	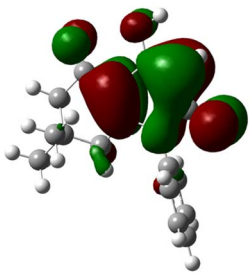	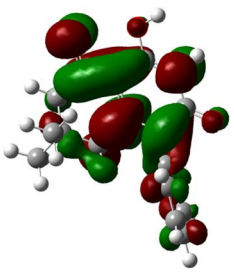

Table 7 (*Contd.*)

Code	Optimized structure	HOMO	LUMO
3g	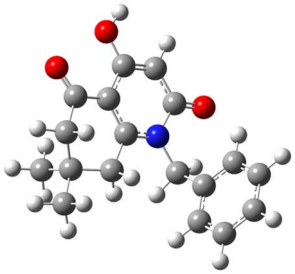	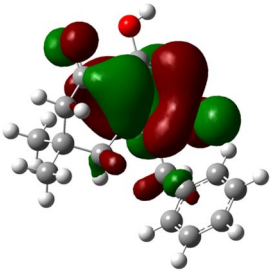	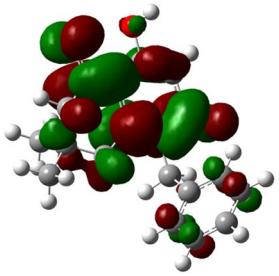
3h	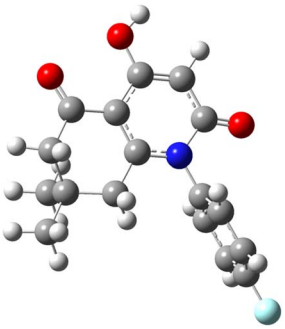	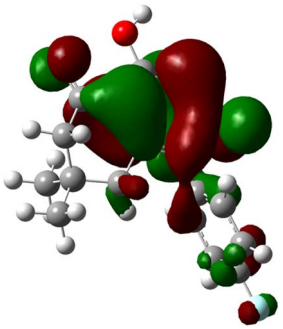	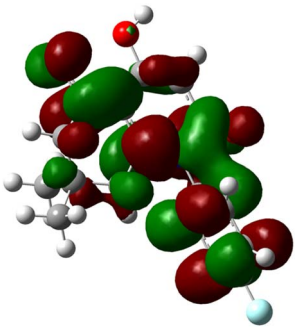
3i	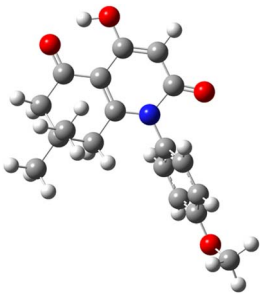	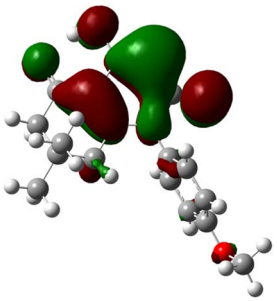	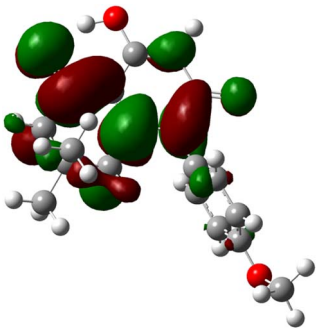
3j	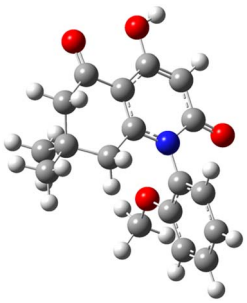	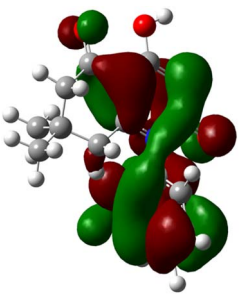	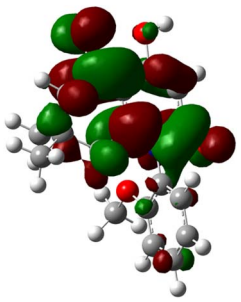

bonds formation. This observation is reliable with the molecular docking results since carbonyl groups were involved in H-bond formation. Moreover, red color corresponding to electron-rich parts of the molecules was also located on the oxygen atom of the hydroxyl group. In addition, blue color that indicates electron-deficient regions was strongly located in hydrogen atoms of the hydroxyl groups suggesting a high electronegativity gap between the two mentioned atoms, thus a significant lability of corresponding hydrogens and the ability of these latter to act as H-bond donors, which was also noticed in molecular docking results in which the hydroxyl group acted as proton donor in H-bond formation with several residues of the corresponding active sites.

Compound **3g** presents a balance between electronic stability and reactivity characterized by a relatively high HOMO–LUMO energy gap of around 4.78 eV. The electronic stability is

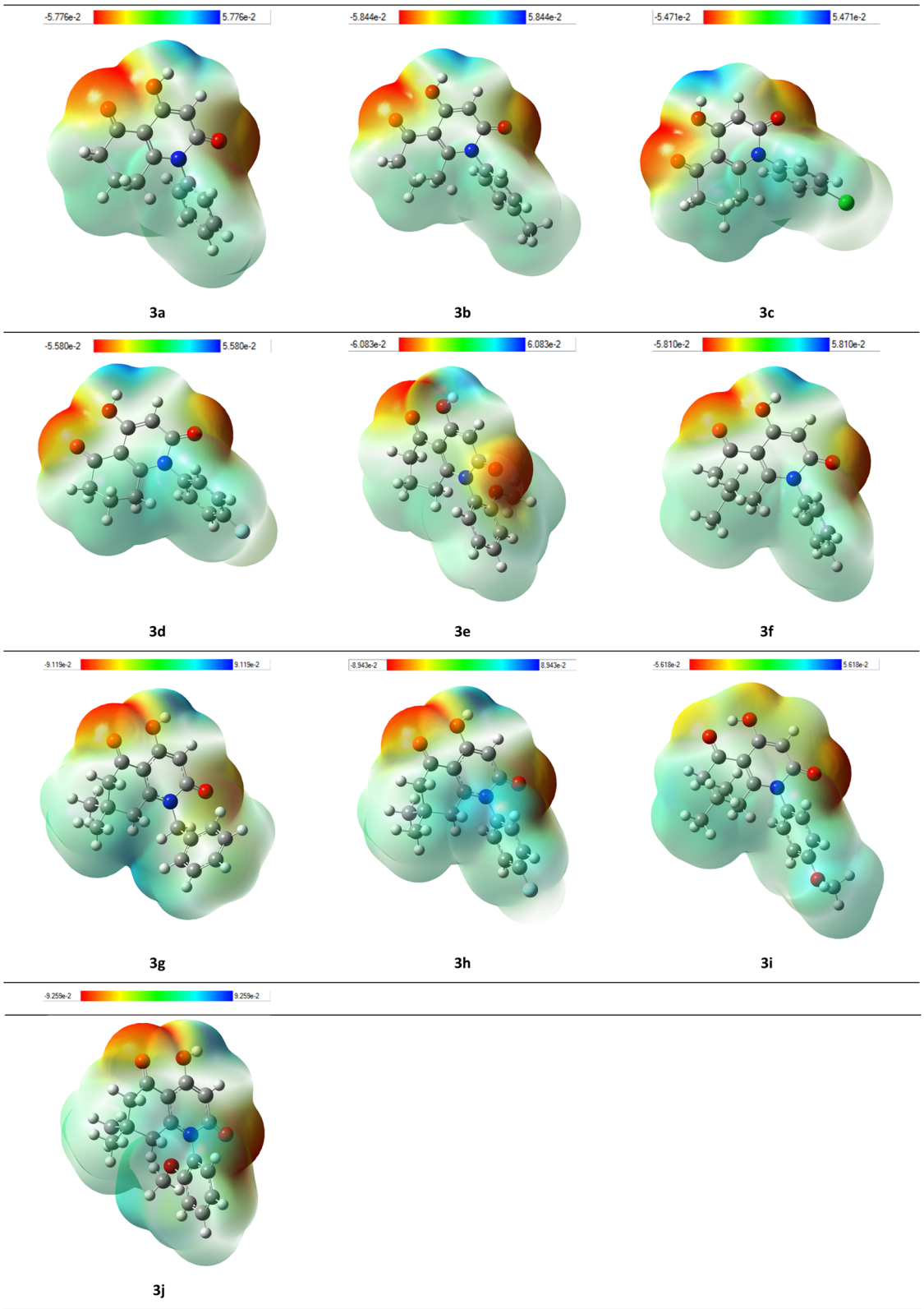

Fig. 9 MEP maps of synthesized 4-hydroxyquinolone analogues.

likely provided by the resonance of the benzyl group as well as the presence of the hydroxyl group that can enhance stability through H-bond formation. On the other hand, the hydroxyl group and the two methyl groups in **3g** contributes in donating electron density to the dihydroquinolone core while the amide and carbonyl functional groups tend to withdraw electron

density, these features are of a great interest in terms of reactivity since it enables the compound to engage in both nucleophilic and electrophilic reactions, in that way, resulting in interactions with specific residues of significant molecular targets.

In view of the DFT results including energy gap as well as the HOMO, LUMO, and MEP representations correlated to the observed interactions in the molecular docking assessment, the main parts of the studied molecules are clearly identified as the functional groups of the nitrogen-based heterocycle especially the hydroxyl group which played the role of an excellent H-bond donor and acceptor. In addition to hydroxyl, the amide and carbonyl groups were also identified as key parts of the molecule participating in the interactions, thereby, contributing to the activity.

Conclusions

Anticancer activity evaluation was performed on synthesized derivatives analogous to 4-hydroxyquinolone core. The synthesis of these products was carried out using a previously reported procedure described by our group involving simple synthons; diethyl malonate and easily prepared β-enaminones. The *in vitro* anticancer activity was evaluated on prepared 4-hydroxyquinolone analogues employing four cancerous cell lines; **HCT116**, **A549**, **PC3**, and **MCF-7**. Results showed that several derivatives of the studied set of compounds were able to inhibit the growth of the aforementioned cell lines especially compound **3g** containing the benzyl group. The molecular docking study that was performed on synthesized products involving known protein kinases; **ALK** and **CDK2** showed promising results with acceptable to good docking scores in which the **3g** derivative was observed as the most potent. The latter exhibiting good docking scores was able to form significant interactions with key residues of the active sites of both **ALK** and **CDK2** owing to the presence of carbonyl and hydroxyl groups within its structure. It is worth-mentioning that the MEP maps generated using DFT identified the carbonyl and hydroxyl groups respectively as the most reactive nucleophilic and electrophilic parts of the molecules. These results displayed a clear consistency between the *in vitro* and *in silico* investigations. This study enabled us to prove once more the importance of β-enaminones as precursors to interesting compounds besides to the high interest of N-heterocycles in drug design. In view of the observed results, it is important to further explore the core of tested 4-hydroxyquinolone analogues in cancer treatment through bringing structural modifications especially on the **3g** derivative, which could enhance the activity while leaning on different *in silico* predictable tools as well as past bibliographic observations.

Data availability

All data generated or analysed during this study are included in this published article and its ESI.† Crystallographic data for **3f** has been deposited at the Cambridge Crystallographic Data Centre CCDC under CCDC 2259912 number and can be obtained from [https://doi.org/10.5517/ccdc.csd.cc2fvmdb].

Author contributions

Y. O. B. synthesis and characterization of compounds, DFT study, manuscript writing, A. B. molecular docking, molecular dynamics simulation, manuscript writing and reviewing, A. D. *in vitro* tests, S. K. B. determining and discussing the anticancer activity, writing and revising the manuscript. M. I. O. analyzed the crystallography data, B. B. contributing to the review of the paper, F. B. contributing to the review of the paper, N. E. A. contributing to the review of the paper.

Conflicts of interest

There are no conflicts to declare.

Acknowledgements

This work was supported financially by The General Directorate for Scientific Research and Technological Development (DG-RSDT), Algerian Ministry of Scientific Research, Applied Organic Chemistry Laboratory (FNR 2000). PRFU Project: B00L01UN230120230002.

Notes and references

1 F. Bray, M. Laversanne, H. Sung, J. Ferlay, R. L. Siegel, I. Soerjomataram and A. Jemal, *Ca-Cancer J. Clin.*, 2024, **74**, 229.
2 M. Siddiqui and S. V. Rajkumar, *Mayo Clin. Proc.*, 2012, **87**, 935.
3 L. Zhong, Y. Li, L. Xiong, W. Wang, M. Wu, T. Yuan, W. Yang, C. Tian, Z. Miao, T. Wang and S. Yang, *Signal Transduction Targeted Ther.*, 2021, **6**, 1.
4 R. Roskoski Jr, *Pharmacol. Res.*, 2024, 107059.
5 (*a*) L. Maram and F. Tanaka, *Org. Lett.*, 2020, **22**, 2751; (*b*) L. Maram and F. Tanaka, *Org. Lett.*, 2019, **21**, 1165.
6 L. Maram, J. M. Michael, H. Politte, V. S. Srirama, A. Hadji, M. Habibi, M. O. Kelly, R. T. Brookheart, B. N. Finck, L. Hegazy, K. S. McCommis and B. Elgendy, *Eur. J. Med. Chem.*, 2025, **283**, 117150.
7 J. Akhtar, A. A. Khan, Z. Ali, R. Haider and M. S. Yar, *Eur. J. Med. Chem.*, 2017, **125**, 143.
8 P. Martins, J. Jesus, S. Santos, L. R. Raposo, C. R. Rodrigues, P. V. Baptista and A. R. Fernandes, *Molecules*, 2015, **20**, 16852.
9 R. V. Patel, Y. S. Keum and S. W. Park, *Eur. J. Med. Chem.*, 2015, **97**, 649.
10 K. Chaudhari, S. Surana, P. Jain and H. M. Patel, *Eur. J. Med. Chem.*, 2016, **124**, 160.
11 B. Sameem, M. Saeedi, M. Mahdavi and A. Shafiee, *Eur. J. Med. Chem.*, 2017, **128**, 332.
12 R. Kaur, L. Dahiya and M. Kumar, *Eur. J. Med. Chem.*, 2017, **141**, 473.

13 N. Kerru, L. Gummidi, S. Maddila, K. K. Gangu and S. B. Jonnalagadda, *Molecules*, 2020, **25**, 1909.
14 X. M. Chu, C. Wang, W. Liu, L. L. Liang, K. K. Gong, C. Y. Zhao and K. L. Sun, *Eur. J. Med. Chem.*, 2019, **161**, 101.
15 S. Jain, V. Chandra, P. K. Jain, K. Pathak, D. Pathak and A. Vaidya, *Arabian J. Chem.*, 2019, **12**, 4920.
16 S. A. Meo, D. C. Klonoff and J. Akram, *Eur. Rev. Med. Pharmacol. Sci.*, 2020, **24**, 4539.
17 J. Zhang, S. Wang, Y. Ba and Z. Xu, *Eur. J. Med. Chem.*, 2019, **174**, 1.
18 D. Sharma, M. Kumar and P. Das, *Synth. Commun.*, 2021, **51**, 2553.
19 M. Kaya, E. Demir and H. Bekci, *J. Enzyme Inhib. Med. Chem.*, 2013, **28**, 885.
20 E. K. Aslan, K. Lam, C. Dengiz, K. Denzinger, I. Y. D. Erdamar, S. Huang, G. W. Zamponi, G. Wolber and M. G. Gündüz, *J. Mol. Struct.*, 2024, **1307**, 137983.
21 G. Periyasami, P. Antonisamy, K. Perumal, A. Stalin, M. Rahaman and A. A. Alothman, *Bioorg. Chem.*, 2019, **90**, 103047.
22 G. M. Sheldrick, *Acta Crystallogr., Sect. A:Found. Adv.*, 2015, **71**, 3.
23 O. V. Dolomanov, L. J. Bourhis, R. J. Gildea, J. A. K. Howard and H. Puschmann, *J. Appl. Crystallogr.*, 2009, **42**, 339.
24 G. M. Sheldrick, *Acta Crystallogr., Sect. C:Struct. Chem.*, 2015, **71**, 3.
25 Rigaku Oxford Diffraction, CrysAlisPro Software System, 2022.
26 C. F. Macrae, I. Sovago, S. J. Cottrell, P. T. A. Galek, P. McCabe, E. Pidcock, M. Platings, G. P. Shields, J. S. Stevens, M. Towler and P. A. Wood, *J. Appl. Crystallogr.*, 2020, **53**, 226.
27 R. Redjemia, A. Bouzina, Y. O. Bouone, A. Mansouri, R. Bahadi and M. Berredjem, *Res. Chem. Intermed.*, 2022, **48**, 4947.
28 Y. O. Bouone, A. Bouzina, R. Sayad, A. Djemel, F. Benaceur, A. Zoukel, M. Ibrahim-Ouali, N.-E. Aouf and F. Bouchareb, *RSC Adv.*, 2023, **13**, 28030.
29 D. A. Sabbah, S. E. Hasan, R. Abu Khalaf, S. K. Bardaweel, R. Hajjo, K. M. Alqaisi, K. A. Sweidan and A. M. Al-Zuheiri, *Molecules*, 2020, **25**, 5348.
30 (*a*) N. Teggar, B. Bakchiche, M. E. S. Abdel-Aziz, S. K. Bardaweel and M. A. Ghareeb, *Jordan J. Pharm. Sci.*, 2023, **16**, 184; (*b*) L. Alsous and S. Bardaweel, *Adv. Anticancer Agents Med. Chem.*, 2022, **22**, 1826.
31 M. Menichincheri, E. Ardini, P. Magnaghi, N. Avanzi, P. Banfi, R. Bossi, L. Buffa, G. Canevari, L. Ceriani, M. Colombo, L. Corti, D. Donati, M. Fasolini, E. Felder, C. Fiorelli, F. Fiorentini, A. Galvani, A. Isacchi, A. L. Borgia, C. Marchionni, M. Nesi, C. Orrenius, A. Panzeri, E. Pesenti, L. Rusconi, M. B. Saccardo, E. Vanotti, E. Perrone and P. Orsini, *J. Med. Chem.*, 2016, **59**, 3392.
32 D. J. Wood, S. Korolchuk, N. J. Tatum, L. Z. Wang, J. A. Endicott, M. E. M. Noble and M. P. Martin, *Cell Chem. Biol.*, 2019, **26**, 121.
33 Release S, 2 LigPrep, version 3.4. Schrödinger, LLC, New York, NY, 2015, 26400175.
34 R. A. Friesner, J. L. Banks, R. B. Murphy, T. A. Halgren, J. J. Klicic, D. T. Mainz, M. P. Repasky, E. H. Knoll, D. E. Shaw, M. Shelley, J. K. Perry, P. Francis and P. S. Shenkin, *J. Med. Chem.*, 2004, **47**, 1739.
35 (*a*) E. C. Meng, T. D. Goddard, E. F. Pettersen, G. S. Couch, Z. J. Pearson, J. H. Morris and T. E. Ferrin, *Protein Sci.*, 2023, **32**, 4792; (*b*) E. F. Pettersen, T. D. Goddard, C. C. Huang, E. C. Meng, G. S. Couch, T. I. Croll, J. H. Morris and T. E. Ferrin, *Protein Sci.*, 2021, **30**, 70.
36 (*a*) K. J. Bowers, E. Chow, H. Xu, R. O. Dror, M. P. Eastwood, B. A. Gregersen, J. L. Klepeis, I. Kolossvary, M. A. Moraes, F. D. Sacerdoti, J. K. Salmon, Y. Shan and D. E. Shaw, *Proceedings of the ACM/IEEE Conference on Supercomputing (SC06)*, Tampa, Florida, 2006, November 11-17; (*b*) Schrödinger Release 2024-3: Desmond Molecular Dynamics System, D. E. Shaw Research, New York, NY, 2024.
37 Schrödinger Release 2023-4: Maestro, Schrödinger, LLC, New York, NY, 2024.
38 (*a*) A. D. Becke, *J. Chem. Phys.*, 1993, **98**, 5648; (*b*) M. M. Francl, W. J. Pietro, W. J. Hehre, J. S. Binkley, M. S. Gordon, D. J. DeFrees and J. A. Pople, *J. Chem. Phys.*, 1982, **77**, 3654.
39 M. J. Frisch, *Gaussian-09 Revision A.02*, Gaussian Inc, Wallingford CT, 2009.
40 G. Zhang and C. B. Musgrave, *J. Phys. Chem. A*, 2007, **111**, 1554.
41 A. Bouzina, M. Berredjem, B. Belhani, S. Bouacida, C. Marminon, M. Le Borgne, Z. Bouaziz and M. Aissaoui, *Res. Chem. Intermed.*, 2021, **47**, 1359.
42 A. Bouzina, Y. O. Bouone, O. Sekiou, M. Aissaoui, T. S. Ouk, A. Djemel, R. Mansouri, M. Ibrahim-Ouali, Z. Bouslama and N. E. Aouf, *RSC Adv.*, 2023, **13**, 19567.
43 A. Bouzina, A. Djemel, O. Sekiou, I. Kadi, Y. O. Bouone, R. Mansouri, Z. Aouf, M. Ibrahim-Ouali and N.-E. Aouf, *J. Mol. Struct.*, 2023, **1285**, 135527.
44 I. J. Amaye, R. D. Haywood, E. M. Mandzo, J. J. Wirick and P. L. Jackson-Ayotunde, *Tetrahedron*, 2021, **83**, 131984.
45 Y. O. Bouone, A. Bouzina, N.-E. Aouf and M. Ibrahim-Ouali, *Res. Chem. Intermed.*, 2023, **49**, 1349.
46 R. Roskoski Jr, *Pharmacol. Res.*, 2017, **117**, 343.
47 R. Roskoski Jr, *Pharmacol. Res.*, 2013, **68**, 68.
48 S. Ghafouri-Fard, T. Khoshbakht, B. M. Hussen, P. Dong, N. Gassler, M. Taheri, A. Baniahmad and N. A. Dilmaghani, *Cancer Cell Int.*, 2022, **22**, 325.